processes

MDPI

Article

Study and Analysis of Corrosion Rate, Hot Tensile Properties, and Metallurgical Changes of SSDS 2507 and AISI 316 Dissimilar Weldments

Mamatha Vemulawada [1], Megersa Olumana Dinka [2], Abhishek Agarwal [3,*], Masengo Ilunga [4], Balram Yelamasetti [5,*], Srinivasa Vadayar K [6] and Naveen Kumar P [5]

1 Department of Metallurgical Engineering, JN Government Polytechnic, Hyderabad 500013, Telangana, India; jngpmamatha@gmail.com
2 Department of Civil Engineering Science, University of Johannesburg, APK Campus, Johannesburg 2006, South Africa; mdinka@uj.ac.za
3 Department of Mechanical Engineering, College of Science and Technology, Royal University of Bhutan, Phuentsholing 21101, Bhutan
4 Department of Civil Engineering, University of South Africa, Pretoria 1709, South Africa
5 Department of Mechanical Engineering, MLR Institute of Technology, Hyderabad 500043, Telangana, India
6 Department of Metallurgical Engineering, Jawaharlal Nehru Technological University Hyderabad, University College of Engineering, Science & Technology Hyderabad, Hyderabad 500085, Telangana, India
* Correspondence: agarwala.cst@rub.edu.bt (A.A.); balram3072@gmail.com (B.Y.)

Abstract: This research study aims to study and investigate the corrosion rate, hot tensile properties, and microstructures of SSDS 2507 and AISI 316 gas tungsten arc dissimilar weldments. Three separate samples were developed with frequencies of 2, 4, and 6 Hz using the pulse arc mode technique. The tensile characteristics were assessed at two distinct temperatures (27 °C and 350 °C) in order to examine the behavior of the welded structure. Mechanical characterization such as hardness measurement and corrosion behavior were studied. The metallurgical characteristics of pulsed and continuous current weldments were examined using microscopes (optical and scanning), revealing variations across different zones. At the 4 Hz pulse frequency, the material exhibited improved tensile qualities compared to constant arc welding. The microstructures indicated that the fusion zone in the pulsed arc weldment consisted of a balanced mixture of inter-granular austenite and ferrite phases. A better corrosion resistance rate of 0.0487 mm/year was observed in the pulsed arc weldment compared to both the SSDS2507 base metal and the constant arc weldment. Specifically, at a temperature of 27 °C, the ultimate tensile strength was 695 MPa, whereas at a temperature of 350 °C, the tensile strength was 475 MPa. The weld strength of the pulsed arc weldment exhibited a 15.8% improvement in comparison to the constant arc weldment. The surface hardness value increased to 240 HV compared to the constant arc weldment, which had an HV of 225.

Keywords: constant arc mode; pulse arc mode; SSDS 2507; steel 316; hot tensile test; corrosion test; metallurgical studies

check for updates

Academic Editors: Qunjie Xu and Qingmin Yu

Received: 20 October 2024
Revised: 12 December 2024
Accepted: 6 January 2025
Published: 9 January 2025

Citation: Vemulawada, M.; Dinka, M.O.; Agarwal, A.; Ilunga, M.; Yelamasetti, B.; K, S.V.; P, N.K. Study and Analysis of Corrosion Rate, Hot Tensile Properties, and Metallurgical Changes of SSDS 2507 and AISI 316 Dissimilar Weldments. *Processes* **2025**, *13*, 167. https://doi.org/10.3390/pr13010167

Copyright: © 2025 by the authors. Licensee MDPI, Basel, Switzerland. This article is an open access article distributed under the terms and conditions of the Creative Commons Attribution (CC BY) license (https://creativecommons.org/licenses/by/4.0/).

1. Introduction

The term duplex stainless steels (DSSs) refers to a class of steels with a two-phase ferrite–austenitic microstructure, both of whose constituents are stainless steel; that is, they contain more than 13% Cr [1]. Upon comparing austenitic steels with DSSs, many benefits emerged, including enhanced mechanical strength, enhanced corrosion resistance, and reduced cost due to the reduced nickel content. Because of DSS's exceptional resistance to

chloride-induced corrosion, it is a material of interest in many marine and petrochemical industry applications [2,3]. Mohammed et al. [4] presented a review paper on the effect of heat input rate on the development of dissimilar weldments of austenitic stainless steels and duplex stainless steels. The low cooling rate caused by high input heat furthered the transition of a weld metal with stainless steel from the delta-ferrite phase to the austenite phase [5]. Thus, the final compositions of weld metal austenitic stainless steels exhibited $\gamma + \delta$ structures. The thermal energy input utilized during the welding procedure determined the final ferrite-to-austenite ratio in the final welded structures [6]. Deng et al. [7] investigated corrosion behavior and carried out microstructural studies of lean duplex steels (LDX2101) using the DL-EPR method aged at 700 °C. The microstructural studies revealed that aging LDX2101 at 700 °C resulted in Cr2N precipitation in the α region and then in the γ phase. Zhang et al. [8] studied the impact of aging on lean duplex steels' (2101) ability to resist corrosion at 700 °C. The findings demonstrated that the precipitate-induced microstructure alterations in the duplex stainless steel impacted its resistance to pitting and corrosion. Compared to the potentio-dynamic test, the potentio-static pitting corrosion measurement showed that it was more sensitive to small amounts of precipitates. Han et al. [9] reported on the microstructural changes and corrosion behavior of duplex weldments in different zones. In the heat-affected zone (HAZ), the banded microstructure vanished after welding and changed into coarse equiaxed ferrite grains. The precipitation of Cr2N was observed in some places with a reduced austenite concentration. This resulted in a comparatively decreased resistance to pitting corrosion in the weld root, weld cap, and HAZ. Ouali et al. [10] assessed the impact of heat rate on corrosion and structural changes in lean duplex steel weldments using the gas tungsten arc welding (GTAW) technique with three different heat inputs. Potentio-dynamic polarization tests conducted on several welded joints assessed in a 3.5% NaCl solution demonstrated that the weld metal generated with little heat input had good corrosion resistance. The findings demonstrated that an increased austenite percentage in weld metals led to notable microstructural development with increasing heat input rates.

The third generation of duplex stainless steel is called super duplex stainless steel (SDSS). Nickel and chromium concentrations in SDSS are greater than those in DSS. The corrosion-resistant alloys known as super duplex stainless steels have a balanced, two-phase ferrite and austenite microstructure [11]. Better localized corrosion resistance is provided by the combination of ferrite and austenite in SDSSs as opposed to purely austenitic stainless steels. Between −50 and 250 °C, they provide excellent toughness and strong yield strength [12]. Super DSSs are extensively employed in chemical tankers, the petrochemical sector, the maritime and nuclear power industries, and other industries because of their promising corrosion qualities and high mechanical strength mixed with superior toughness. In some of the aforementioned applications where corrosion cracking due to sulfide or chloride stress is a significant problem, this alloy is a great substitute for austenitic stainless steels [13,14]. Tahchieva et al. [15] revealed microstructural changes under diffusion surface treatments of duplex steels and super duplex steels. Nitrogen diffuses more widely in ferrite, which promotes the development of secondary-phase precipitation, primarily sigma phase, and the dispersion of that precipitation along grain boundaries. Verma et al. [16] demonstrated the different welding processes and their heat input rates on corrosion rate and microstructural changes in duplex stainless steels. The studies revealed that lower ductility, corrosion susceptibility, and solidification cracking are caused by an unbalanced austenite/ferrite phase ratio. Also, it was suggested that extremely high cooling rates, such as 139 °C per second in the pulsed-current GTAW (PCGTAW) method, promote the austenite phase and give the weld the ideal ferrite/austenite ratio.

Welding technology is important in various industries, enabling the joining of diverse materials and structures. The aerospace and automotive industries, in particular, demand precise and reliable welding techniques to ensure the integrity and good performance of critical components [17,18]. Fusion welding entails the melting of the base materials that are to be joined to establish a durable connection between them. Fusion welding involves the application of heat to the edges of a material, causing it to melt and subsequently solidify, resulting in its fusion. This results in a uniform and uninterrupted connection with consistent metallurgical properties throughout the welded area [19]. Gas tungsten arc welding utilizes a tungsten electrode that is not capable of burning to produce the welding arc. GTAW is a highly adaptable welding process that yields welds of superior quality and offers exceptional control over welding parameters. Constant-current GTAW (CCGTAW) provides a consistent welding current, and its stable arc is ideal for welding tasks that need precision and control over heat input. Pulsed-current GTAW changes between high-peak and low-background currents using a pulsed waveform. The pulsation of electric currents enhances the formation of the molten metal pool and improves the amount of heat transferred. PCGTAW provides benefits such as decreased HAZ, reduced distortion, and enhanced weld bead quality. It is frequently selected for applications that involve dissimilar materials and thicker materials that require high precision [20,21].

Devendranath et al. [14] made comparative studies on dissimilar weldments of UNS S32750 and steel 316L developed by duplex and Ni-Cr filler wires. It was observed from metallurgical studies that there were uniform and balanced ferrite and austenite phases in duplex filler weldments. Also, secondary phases with enriched elements like Mo and Nb were observed in ERNiCrMo-03 filler weldments. Ramkumar et al. [22] studied the behavior of dissimilar welds of marine-grade steel (AISI 904L) materials and super duplex steels (UNS S32750) developed with CCGTAW and PCGTAW techniques. Coarse grain structures with ferrite phases in the HAZ of super duplex steels were observed in metallurgical studies using both welding techniques. The corrosion properties seemed to be higher in the base metal (AISI 904L) than those in the both fusion zones. Ramkumar et al. [23] developed dissimilar weldments of UNS S32750 and HSLA steels using a pulsed direct current process using two different fillers (ER80S-Ni3 and ER2553). The samples were fractured under tensile tests at the interface of HSLA steels due to the austenite deformation and segregation of low-density alloying elements from the fillers. The retained austenite and martensite laths seen in the ER80SNi-3 joints' weld microstructure contribute to their higher hardness.

Song et al. [24] modified the GTAW process for cladding austenitic stainless steel 316L in a single pass using varied contact tip-to-work distances (CTWDs) and found that corrosion resistance improved with a CTWD of 5 mm due to ideal ferrite distribution and refined microstructure. High hardness was recorded with a CTWD of 3 mm and it was concluded that adjusting CTWD can improve the corrosion resistance of welded 316L stainless steel. Na et al. [25] studied the impact of welding on thermal deformation in square cells for casks used as nuclear fuel storage. They used STS316L material and used butt welding to partition and connect cells. The results showed substantial thermal deformation in thick-walled columns due to heat conduction distribution fluctuations. Wang et al. [26] studied the corrosion resistance of 904L composite plate pressure vessels in high-temperature and high-pressure gas field environments. They found that the 904L composite plate had lower pitting resistance than the 825 and higher resistance than the 2205 and 825 composite plates. The 625 welding material also outperformed the E385 welding material. The 904L composite plate met the corrosion resistance criteria. Ahmed et al. [27] studied the welding performance of three filler wires, ER4043, ER5356, and FMg0.6, on high-strength AA6011-T6 plates. They found that the ER4043 and FMg0.6 joints had smaller grain sizes in the fusion zone, superior hardness and tensile strength, and exceptional

fatigue resistance. The FMg0.6 joint had the greatest mechanical strength and improved corrosion resistance with post-weld heat treatment.

Ramkumar et al. [28] analyzed the corrosion behavior of A-TIG welding of super duplex steels with three different flux materials (NiO, MoO_3, and SiO_2). The microstructure was exposed to different weldment zones by electrolytic etching. To assess the corrosion characteristics of the welds in a 3.5% NaCl environment, potentio-dynamic polarization measurements were also conducted. Within the fusion zones for all the welded joints, microstructure investigations revealed the production of coarser ferrite grains in addition to three distinct forms of austenite: intra-granular, Widmanstätten, and grain boundary austenite. The results of the research demonstrated that the UNS S32750 had corrosion resistance compared to the welds made using different fluxes. Alwin et al. [29] assessed the phase balance and corrosion cracking for A-TIG and TIG weldments of duplex steels. Since austenite completely dissolves during the weld heat cycle and ferrite grains develop as a result, the HAZ of the TIG weld joint was observed to be greater. Also, the variations in the heat cycle during welding contributed to the observed variations in ferrite content in the weld joints produced by the TIG and ATIG welding processes.

From the literature review, the combination of dissimilar weldments SSDS 2507 and AISI 316 has a wide range of applications in corrosive environments such as in the petro-chemical, marine, and nuclear industries [30]. The current research work focused on the micro-hardness, hot tensile properties, corrosion properties, and metallurgical changes in dissimilar weldments of SSDS 2507 and AISI 316 developed with CCGTAW and PCGTAW techniques. Tensile properties of welded structures were evaluated at a high temperature (350 °C) and room temperature (27 °C). Micro-indentation was made on the weld surface to measure the hardness number using a Vickers hardness tester. The corrosion behavior of the welds was examined using corrosion experiments in an aqueous environment containing 3.5% NaCl. The effect of pulse and constant arc modes on dissimilar weldments was revealed and analyzed in different zones using OM and SEM/EDS microscopes.

2. Materials and Methods

The base materials, SSDS 2507 and AISI 316 (Bhagyashali Metal, Mumbai, India), of 6 mm thickness were used in the present research study. The GTAW technique was adapted to produce dissimilar weld joints with electrodes (ER2205 with a dia. of 1.6 mm). Before welding, the groove angle of 60° with a 1.5 mm root face was considered [2]. The chemical compositions of base metals (BMs) and electrode filler metals are represented in Table 1. The GTAW method with DCSP under the constant-current mode, as well as the pulsed-current mode, was used to weld the dissimilar base metals. The welding process parameters are shown in Table 2. Multiple passes (root pass and cap pass) were considered to join the 6 mm thick plates. During welding, base metals were fixed using a fixture set-up. The three pulse frequencies (2 Hz, 4 Hz, and 6 Hz) were taken to study the effect of pulse frequency by keeping a constant peak current (Ip-140 A) and a constant background current (Ib-80 A) [2]. In constant arc mode, the peak current of 140 A was taken to compare the welding characteristics of constant and pulse arc modes in the GTAW process. The weldments developed with both welding arc modes are shown in Figure 1.

Table 1. The chemical composition of BMs and filler wire [31].

Metals	Cr	Ni	Mo	Si	Mn	Cu	P	S	N	C
SSDS 2507	24–26	6–8	3–5	0.08	1.20 max	0.50 max	0.035	0.02 max	0.24–0.32	0.03 max
AISI316	16–18	10–14	2–3	0.75 max	2 max	--	0.045	0.030	0.10	0.08
ER2205Filler	21–23	4.5–6.5	2.5–3.5	1.0 max	2.00 max	--	0.30	0.020	0.20	0.03 max

Table 2. The welding process parameters.

Sample ID	PCGTAW		PCGTAW		PCGTAW		CCGTAW	
Parameter	**1st Pass**	**2nd Pass**	**1st Pass**	**2nd Pass**	**1st Pass**	**2nd Pass**	**1st Pass**	**2nd Pass**
Peak current (Ip), A	140	140	140	140	140	140	140	140
Background current (Ib), A	80	80	80	80	80	80	-	-
Frequency, (Hz)	2	2	4	4	6	6	-	-
Voltage, (V)	24–26	24–26	24–26	24–26	24–26	24–26	25–28	25–28
Argon gas rate (lpm)	15	15	15	15	15	15	15	15



Figure 1. Welded samples were developed using pulsed and constant arc modes in GTAW.

Characterization

After the welding processes, the weldments were sliced into different welding coupons, as shown in Figure 2, to characterize the weld properties. Sample preparation for microstructural examination was conducted in accordance with ASTM E3-95 [32]. The samples underwent polishing using emery papers with varying levels of silicon carbide grit (180, 400, 600, 800, 1200, 1500), followed by the application of alumina suspension. Finally, diamond polishing was conducted to achieve a pristine and lustrous surface. The polished weldments were treated with Kallings reagent for 20–30 s to obtain metallographic pictures using optical microscopy [14]. The BX51M-LED OLYMPUS microscope (Labline Stock Centre, Mumbai, India) was utilized to acquire optical micrographs. The corrosion performance of welded samples was assessed by a potentio-dynamic polarization test according to the ASTM B117 [33,34] criteria. The set-up for the electrochemical test included an SCE that served as a reference electrode. The samples being tested acted as the working electrode, while a platinum wire was used as the counter electrode.

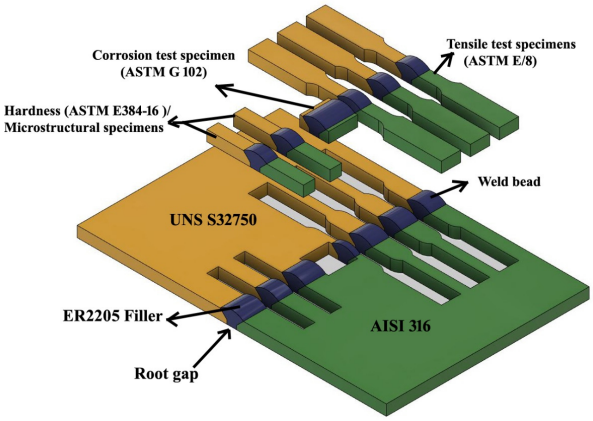


Figure 2. Tensile ASTM standards (tensile, corrosion, hardness, and microstructure).

The test was conducted using a scanning rate of 1 millivolt per second. The specimens were submerged in a 3.5% sodium chloride solution prepared using distilled water for a duration of 30 min at ambient temperature. The surfaces of the specimen that were immersed in the solution maintained a consistent area of 0.1257 cm^2. The electrolyte used was a 3.5% NaCl solution, the reference electrode was an Ag/AgCl electrode, and the counter electrode was a platinum wire [35]. The corrosion potentials were calculated by extrapolating the linear segments of the anodic as well as cathodic curves to determine the corrosion current densities. The corrosion current density was determined within the range of ECorr = ±25 mV using the Stern–Geary equation. The tensile coupons were assessed using a Universal Testing Machine (UTM) (Fuel Instruments and Engineers Pvt. Ltd, Maharashtra, India). The weldments with ASTM E8 standard samples were subjected to tensile testing. Tensile experiments were conducted at a strain rate of 0.004/s. The HVs were determined by using a Vickers micro-hardness tester on the surface area of the weld. A load capacity of 500 gf and a dwell length of 10 s was consistently maintained throughout the measurement. The test was conducted in accordance with the ASTM E384-16 [36] standard.

3. Results

3.1. Metallurgical Studies

3.1.1. Microstructures of Base Metals

Figure 3a–d display the microstructure of the base metal for SSDS 2507 and AISI 316, together with its corresponding SEM image. The microstructure was characterized as a conventional two-phase structure, consisting of alternating austenite as well as ferrite phases, and the austenite phase (γ) was observed in the light region, while ferrite (δ) seemed darker. The grains of ferrite and austenite in SDSS 2207 were stretched in the rolling direction, as depicted in Figure 3a,b. The austenitic grain structure for steel is depicted in Figure 3c,d. The optical macrostructure of PCGTAW −4 Hz and CCGTAW weldments is shown in Figure 4. The macrographs show the uniform distribution of filler alloying elements in both welding techniques. Figure 4a shows the CCGTAW weldment macrostructure along with the bead profile where the root pass filament depth seems to be more than the PCGTAW weldment, as shown in Figure 4b. Also, clear bead formation with minimal bead height was observed in the PCGTAW technique compared to that in the CCGTAW technique.

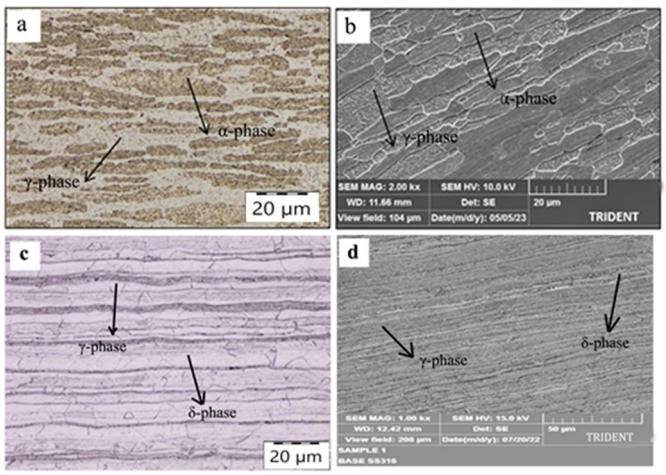


Figure 3. OM/SEM microstructures of base metal (**a**,**b**) SSDS 2507 (**c**,**d**) AISI 316.

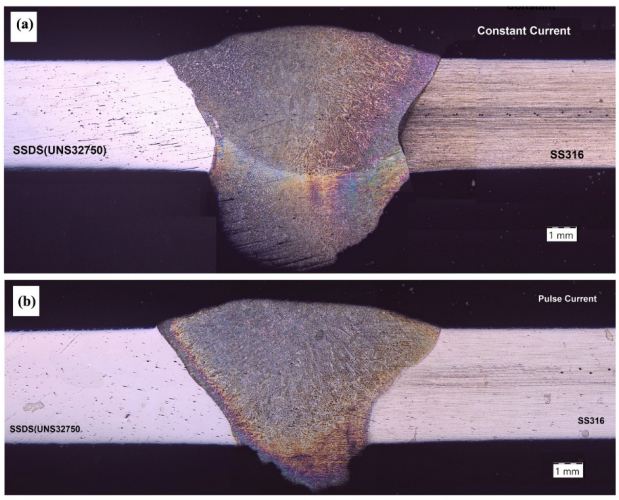


Figure 4. The optical macrostructures of weldments with (**a**) constant current and (**b**) pulsed current.

3.1.2. Microstructures of Dissimilar CCGTAW Weldments

The optical micrographs of CCGTAW weldments are shown in Figure 5. The microstructures were captured with different magnifications in different zones of weldment. Figure 5a shows the interface of SDSS 2507 to the weld zone where coarse ferrite grains occurred due to the inadequate phase formation of GBA from the SDSS side. Figure 5b shows the weld area of the CCGTAW weldment which shows both the reformed austenite phase (γ) and the ferrite phase (δ). Continuous heat was maintained to form the austenite phase in the weld zone. Figure 5c shows that with an increase in the heat input, the microstructure of the steel 316 HAZ exhibited increased grain morphology between the base metal and another material. Grain coarsening could be seen on the AISI 316 side. Also, it led to the formation of secondary phases and the segregation of alloying elements attributed to failure under uni-axial loading conditions [37].

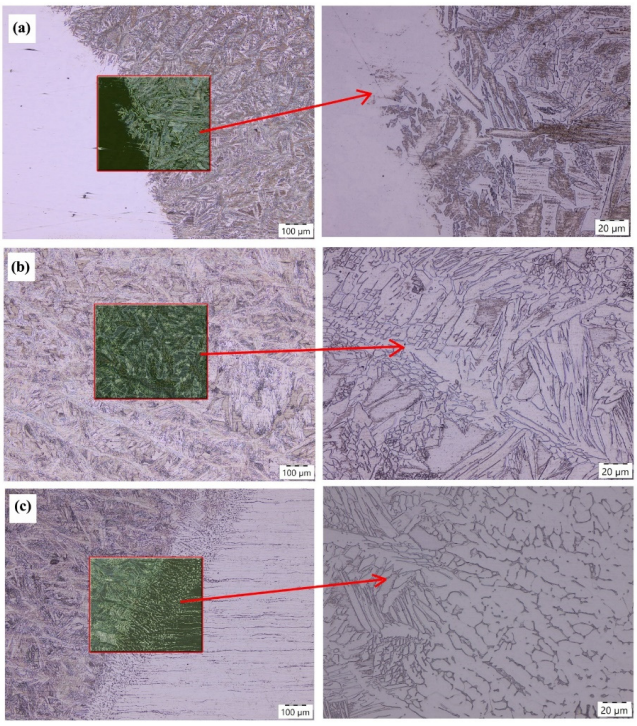


Figure 5. CCGTAW micrographs of (**a**) SSDS 2507, (**b**) weld zone, and (**c**) AISI 316.

The interface of both the base metals and their HAZ width of the CCGTAW weldment are shown in Figure 6. The HAZ width of SSDS S32750 (Figure 6a) was observed as 403.77 µm, whereas 458.22 µm was observed on the AISI 316 side (Figure 6b). Due to the lower thermal conductivity rate in AISI 316 material, a higher HAZ width was observed as compared with that of the SSDS 2507 material. More heat accumulated on the AISI 316 side than on the duplex steel side due to continuous heat input, which could be attributed to the development of thermal gradients that resulted in new phase formation and micro-segregation of alloying elements at the interfaces of both the base metals. Also, it could be seen from the micrographs of HAZs that the segregation of lower-density alloying elements was higher on the AISI 316 side than the SSDS 2507 side. In the SSDS 2507 HAZ, interface microstructures revealed a little grain coarsening (Figures 5a and 6a) and the existence of delta ferrite stringers in the HAZ of AISI 316L (Figures 5c and 6b). The creation of new, larger ferrite grains occurred due to the inadequate establishment of the GBA phase on the side of the SDSS and the coarsening of grains in AISI 316. With continual heat input, coarse grain structures with cellular grains were observed. The weld zone exhibited higher amounts of austenite phases than the HAZ of steel [38].

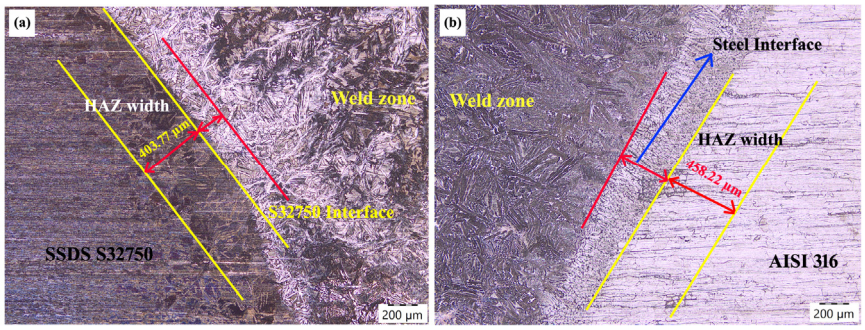


Figure 6. Typical microstructures showing the HAZ width of CCGTAW weldment: (**a**) SDSS 2507 and (**b**) AISI 316.

Weld zone OM/SEM micrographs of the CCGTAW weldment are illustrated in Figure 7. They show the presence of various forms of austenite, including wedge-shaped Widmanstätten austenite; needle-shaped, elongated grains of austenite; and inter-granular precipitates that start from ferrite phases. As a result of continual heat input, coarse grain structures with cellular grains were observed. The weld zone exhibited higher amounts of austenite phases than the HAZ of steel. With an increase in heat input, austenite phases increased in the weld zone, and this is ascribed to increasing HV. EDS point analysis was performed at various weldment positions, as shown in Figure 8. The peaks corresponding to the principal alloying elements were observed, and the weight of these elements is provided in Table 3. It was observed that the constituents, Ni, Cr, Mo, and Fe, were enhanced at the interface of the SDSS 2507 side (Figure 8a) and AISI 316 side (Figure 8c). Also, the fusion zone dark phases showed an enrichment of Ni, Fe, and Cr (Figure 8b). Elemental movement was observed in the HAZ of steel 316 from the weld zone. Similar observations were observed in researcher findings when duplex and super duplex steels joined with steel materials.

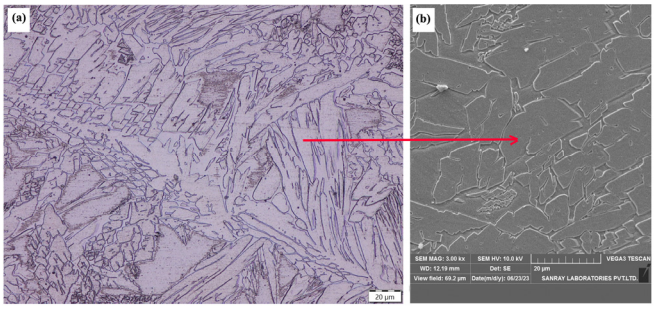


Figure 7. Weld zone of CCGTAW: (**a**) OM micrograph and (**b**) SEM micrograph.

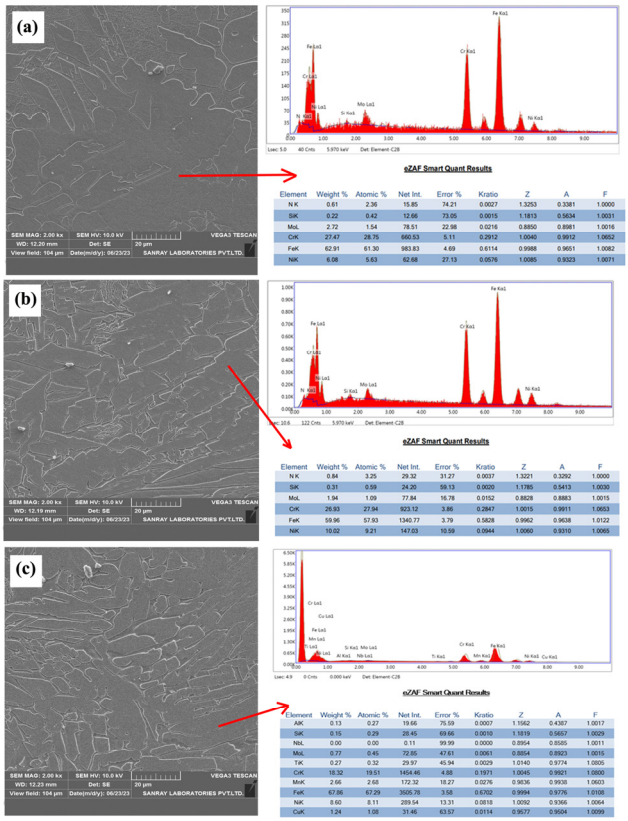


Figure 8. SEM/EDS point analysis of CCGTAW weldment in HAZ of (**a**) SSDS 2507, (**b**) weld zone, and (**c**) AISI 316.

Table 3. EDS point analysis in various zones of CCGTAW weldment—major alloying elements.

Zone	Cr	Ni	Fe	Mo	Mn	Si
HAZ of SSDS 2507	27.47	6.08	62.91	2.72	0.81	0.22
HAZ of AISI 316	18.32	8.60	67.86	0.77	2.66	0.15
Weld zone	26.13	10.02	59.96	1.94	0.79	0.31

3.1.3. Microstructures of Dissimilar PCGTAW Weldments

The optical micrographs of PCGTAW weldments are shown in Figure 9. The microstructures were captured with different magnifications in different zones of weldments. Figure 9a shows the interface of SSDS 2507 to the weld zone where balanced ferrite–austenitic grains were observed due to the sufficient GBA phase formation from SSDS 2507. Figure 9b, which shows the weld area of the PCGTAW weldment, reveals both ferrite-austenite phases (γ) with balanced phase structures. Due to the controlled and low pulse frequency (4 Hz), fine and clear needle-like structures were identified in the weld zone. Figure 9c shows the microstructure of the steel AISI 316 HAZ, which exhibited fine grain morphology and less segregation effect. The grain coarsening in PCGTAW was tiny

on the AISI 316 side due to proper heat input rates. In the PCGTAW weldment, delta ferrite stringers were clustered in the AISI 316 HAZ. During the cooling process of welding, the GBA phase first formed at the boundaries of ferrite grains. This was then followed by the growth of secondary austenite in the Widmanstätten structure, which extended to the ferrite grains at specific angles. The ultimate microstructure was established through the level of undercooling. No carbides or intermetallic compounds were detected in the microstructures of both weldments [39].

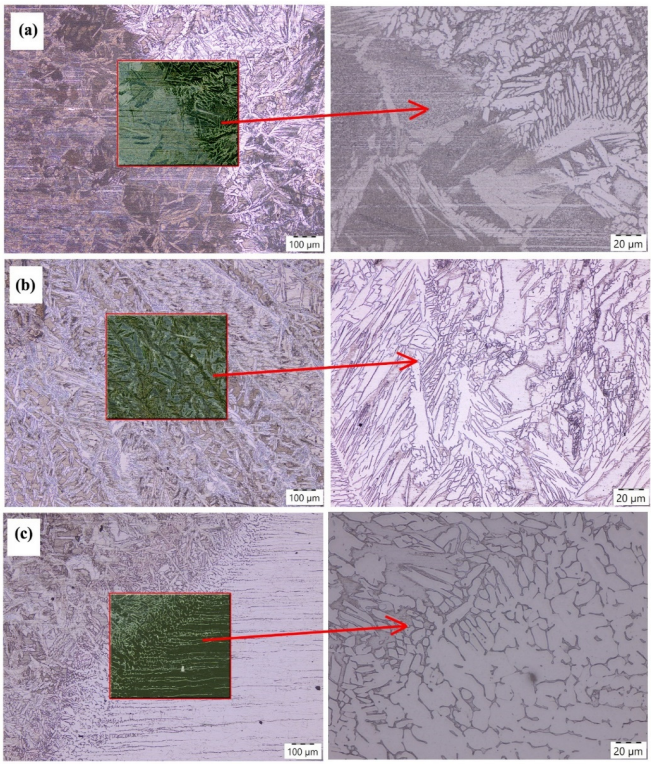


Figure 9. PCGTAW micrographs in HAZ of (**a**) SSDS 2507, (**b**) weld zone, and (**c**) AISI 316.

The interface of both the base metals and their HAZ width of the PCGTAW weldment are shown in Figure 10. The HAZ width of SSDS S32750 (Figure 10a) was observed as 201.47 µm, whereas 230.658 µm was observed on the AISI 316 side (Figure 10b). Due to the lower thermal conductivity rate in the AISI 316 material, a higher HAZ width was observed as compared with the SSDS 2507 material. As compared with the CCGTAW weldment, the HAZ width was greatly reduced in both base metals due to the pulse arc effect between the peak and background current. The segregation of lower-density alloying elements was controlled on the AISI 316 side. In the SSDS 2507 HAZ, interface microstructures revealed no grain coarsening (Figures 9a and 10a) and the existence of delta ferrite stringers in the HAZ of AISI 316 (Figures 9c and 10b), as in the CCGTAW weldment.

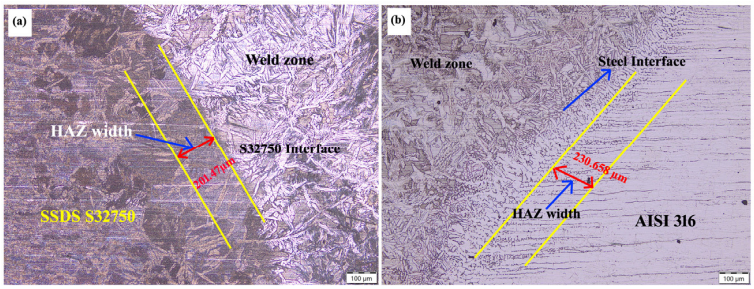


Figure 10. Typical microstructures showing the HAZ width of PCGTAW weldment: (**a**) SSDS 2507 and (**b**) AISI316.

The weld zone OM/SEM micrographs of the PCGTAW weldment are shown in Figure 11. The fusion zone revealed multidirectional grain growth in both columnar and cellular dendrites (Figure 11a). White phases were apparent as splats close to the fusion zone, as shown by SEM analysis of the microstructure (Figure 11b). The fusion border was clearly defined, with distinct grain patterns, and there were no subsequent phases visible. EDS point analysis was performed in various zones, as shown in Figure 12. Peaks corresponding to the principal alloying elements were distinctly observed, and the weights of these elements are provided in Table 4. It was observed that the constituents Fe, Cr, Ni, and Mo were enhanced at the interface of the SSDS 2507 side (Figure 12a). In the fusion zone (Figure 12b), the secondary phases appeared as small, white splats and had higher concentrations of Nb, Ni, and Mo. Conversely, the fusion boundary at AISI 316 (Figure 12c) exhibited the presence of Fe, Cr, and Ni. The migration of Fe from SSDS 2507 and AISI 316 to the weld area was less than that observed in the CCGTAW weldment.

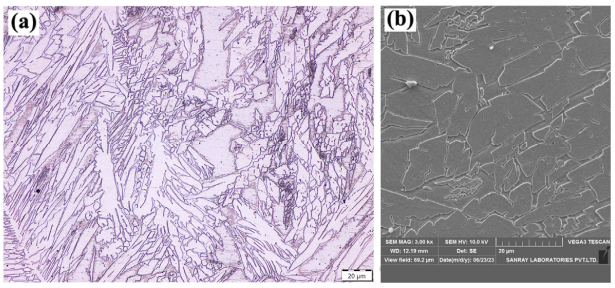


Figure 11. Weld zone of PCGTAW weldment: (**a**) OM micrograph and (**b**) SEM micrograph.

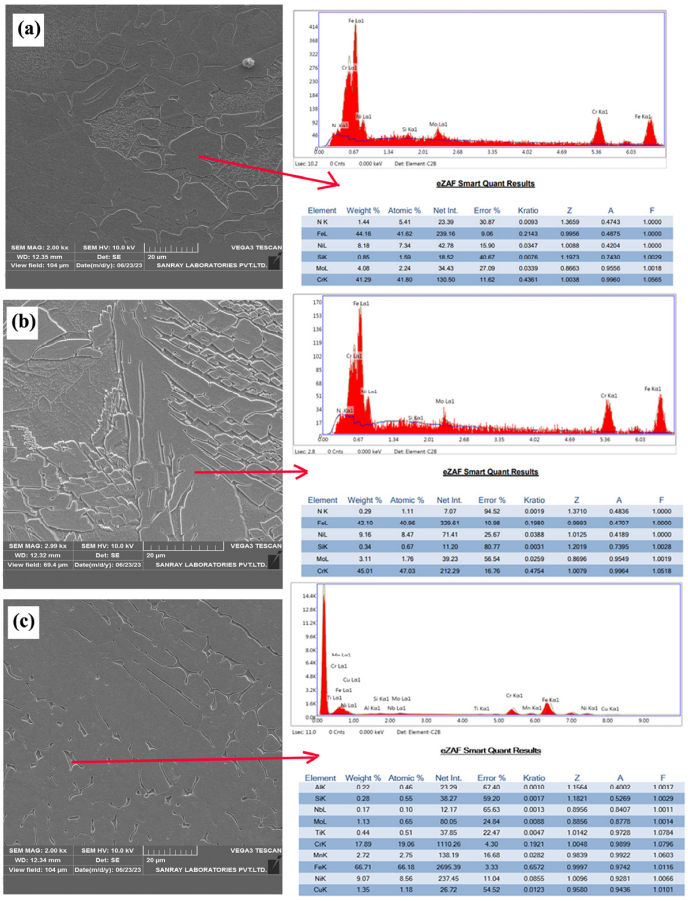


Figure 12. SEM/EDS point analysis of PCGTAW weldment: (**a**) HAZ of SSDS 2507, (**b**) weld zone and (**c**) HAZ of AISI 316.

Table 4. EDS point analysis in various zones of PCGTAW weldment—major alloying elements.

Zone	Cr	Ni	Fe	Mo	Mn	Si
HAZ of SSDS 2507	23.14	8.18	44.16	4.08	0.91	0.85
HAZ of AISI 316	17.89	9.07	66.71	1.33	2.72	0.28
Weld zone	25.22	9.16	42.10	1.88	0.69	0.34

3.2. Corrosion Test

The Tafel curves of BMs, CCGTAW, and PCGTAW welded samples are shown in Figure 13. The corrosion results such as pitting potential (Epit.), corrosion current (Icorr.), and corrosion rate are summarized in Table 5. For all tested samples, the Ecorr. values are rather comparable (from −76.6 mV (BM 2207) to −122 mV (CC)). The results, as demonstrated in Table 5, show that, at −77.25 mV, the Ecorr. value of the PCGTAW process is also close to that of BM, meaning welding does not significantly change the electrochemical stability of a material. Hence, PCGTAW has the most superior Icorr., showing an even lesser value for anodic dissolution in comparison with other samples. The diminished Icorr. signifies the improved stability of the passive coating, which efficiently shields the substrate from additional corrosion. The Epit. of the PCGTAW specimen (342 mV) is higher than that of BM SS316 (229 mV), BM 2207 (234 mV), and CC (326 mV). The higher Epit. indicates enhanced resistance against localized pitting which is associated with a better microstructure and the homogeneity of alloying elements. This procedure decreases the formation of harmful intermetallic phases, such as the sigma phase, prevalent in high-heat-input processes like CC. Moreover, the improved secondary austenite phase in PCGTAW guarantees a consistent distribution of elements such as molybdenum, chromium, and nitrogen, essential ingredients for preventing pitting and crevice corrosion. Under PCGTAW, the Ipass (0.0176 mA/cm^2) is markedly lower than that of other samples, underscoring its exceptional capacity to sustain passivity across a broad spectrum of potentials. And also, the BM and CC samples demonstrate elevated passive current densities, signifying reduced passive film protection. Compared with the BMs, although CC had the lowest corrosion rate (1.3389 mm/yr), it was still within an order of magnitude lower than that of PCGTAW (0.0487 mm/yr), which demonstrates the ability of pulsed welding to mitigate general corrosion, as well as highlighting how detrimental effects can erode at low levels using non-optimal welding processes. The improved performance of PCGTAW is due to its moderate heat input which prevents excessive grain growth and obtains finer microstructure [26]. The potentio-dynamic polarization curve with the highest pitting potential demonstrates superior resistance to pitting corrosion. Observations revealed that the application of reduced heat input (PCGTAW) led to the attainment of the highest pitting potential. This phenomenon occurred because of the creation of a higher secondary austenite phase with low levels of chromium in the samples welded using the PCGTAW process [27].

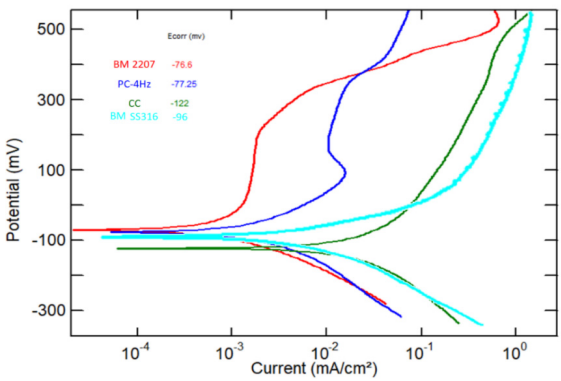


Figure 13. Polarization curves of base metals and PCGTAW and CCGTAW weldments.

Table 5. Corrosion data from potentio-dynamic polarization curves.

Sample	SSDS 2507	AISI 316	PC-4HZ	CC
Ecorr (mv)	−76.6	−96	−77.25	−122
Icorr (mA/cm^2)	0.0535	0.0411	0.0045	0.1251
Epit (mv)	234	229	342	326
Ipass (mA/cm^2)	1.2521	1.1147	0.0176	0.516
Corrosion rate (mm/yr)	0.5729	0.3677	0.0487	1.3389

3.3. Hot Tensile Properties

The test was conducted at room temperature (27 °C) and under hot conditions at 350 °C, and the average data obtained are tabulated in Table 6. The test samples at room temperature before and after fracture are shown in Figure 14. The weld strengths of developed weldments at pulse frequencies 2 Hz, 4 Hz, and 6 Hz were compared with constant-current weldments. In all the conditions, the welding samples were fractured on the steel AISI 316 side. It is perceived from the data that the average UTS values of PCGTA weldments were 645 MPa, 690 MPa, and 610 MPa for 2 Hz, 4 Hz, and 6 Hz pulse weldments, respectively (as shown in Figure 14). For the CCGTA weldment, the UTS value of 600 MPa was observed, which was lower than that of the PCGTA weldments due to the pulse arc mode being maintained with pulse frequencies. The welding strength of PCGTAW at 6 Hz was observed as a little higher than the welding strength of CCGTA weldments due to the higher pulse frequency which produced a constant heat input rate. The pulse frequency at 4 Hz produced a higher-strength welded joint which increased by 15.8% compared to the CCGTA weldments. The YS values of of 2 Hz, 4 Hz, and 6 Hz weldments were observed as 381, 360, and 310 MPa, respectively, which were higher than the YS values of the CCGTA weldment (258 MPa). The ratios of YS to UTS at 2 Hz, 4 Hz, and 6 Hz were observed as 0.59, 0.51, and 0.50, respectively, which were higher than the CCGTA weldments (0.43). Higher yield strength values were observed when the weldments were developed using the PCGTAW technique.

Table 6. The average tensile test values at room temperature.

Sample ID	SSDS 2507-AISI 316 (CC)	SSDS 2507-AISI 316 (PC-2 Hz)	SSDS 2507-AISI 316 (PC-4 Hz)	SSDS 2507-AISI 316 (PC-6 Hz)
Yield strength in MPa	258	381	360	310
Tensile strength in MPa	600	640	695	610
Fitted strain	26	25	29	28
% Reduction in area	75.3	25.8	27.3	59.7
Failure location	AISI 316 HAZ	AISI 316 HAZ	AISI 316 HAZ	AISI 316 HAZ

The tensile properties were evaluated at 350 °C for CCGAW and PCGTAW (4 Hz) weldments, and the test specimen before and after fracture is shown in Figure 15. The results obtained from the test are tabulated in Table 7. It is perceived from the data that the UTS values of the PCGTAW and CCGTAW weldments are 475 and 456 MPa, respectively (as shown in Figure 16). Similarly to room-temperature conditions, the base metal steel 316 side exhibited fracture under tensile loading at increased temperature. The ratio of YS to UTS at 4 Hz pulse frequency was observed as 0.53, which was higher than the CCGTA weldments (0.50) and room-temperature CCGTAW weldments (0.43).

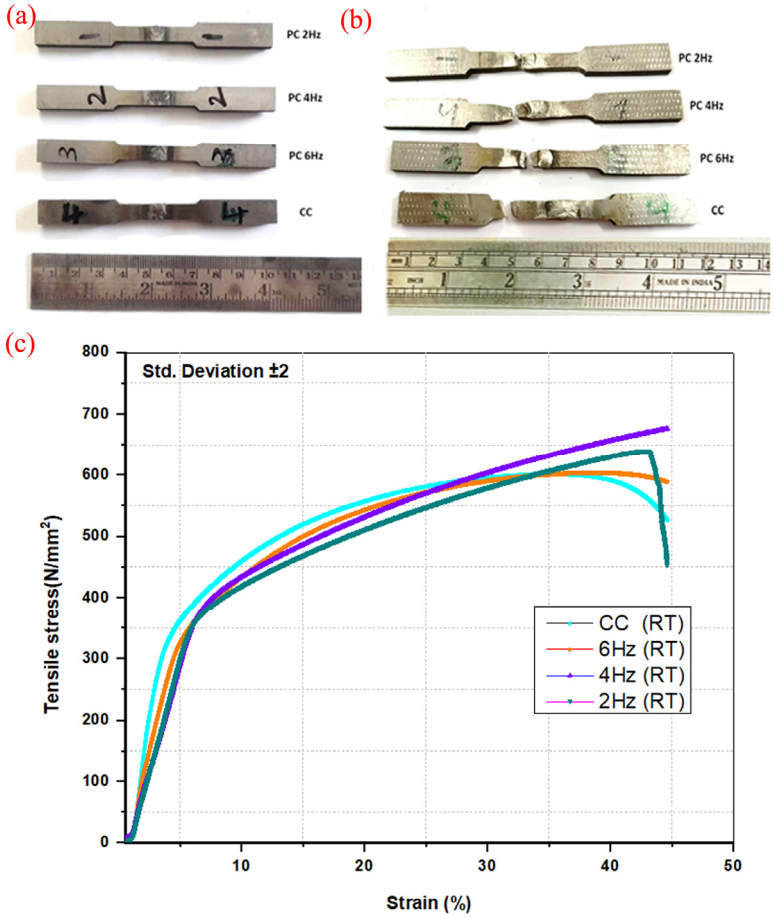


Figure 14. Tensile test samples of CCGTAW and PCGTAW weldments at room temperature: (**a**) before fracture, (**b**) after fracture, and (**c**) stress–strain graph.

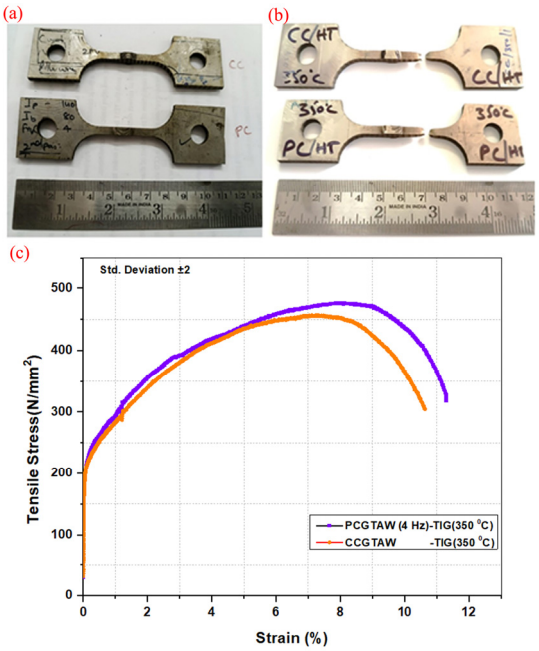


Figure 15. Tensile test samples of CCGTAW and PCGTAW weldments at 350 °C temperature: (**a**) before fracture, (**b**) after fracture, and (**c**) stress–strain graph.

Table 7. The tensile test average values at a temperature of 350 °C.

Sample ID	Yield Strength, MPa	Tensile Strength, MPa	% of Elongation	% of Reduction in Area	Failure Location
SSDS 2507-AISI 316 (CC)	231	456	20	65.8	AISI 316 HAZ
SSDS 2507-AISI 316 (PC-4 Hz)	253	475	21	60.5	

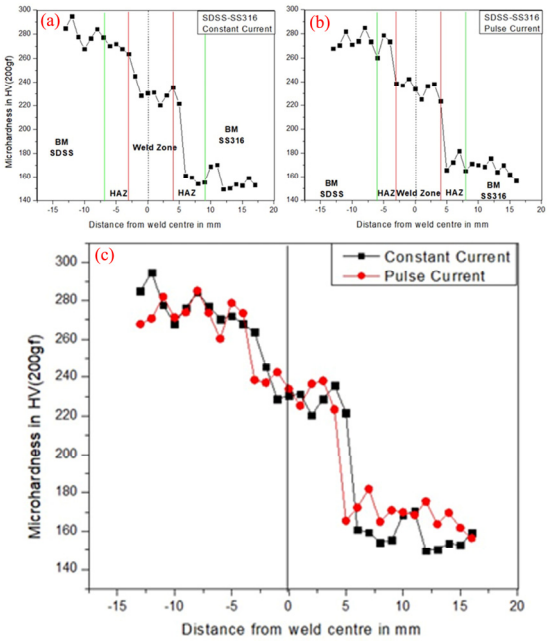


Figure 16. Micro-hardness profile along the transverse direction: (**a**) CCGTAW, (**b**) PCGTAW (4 Hz), and (**c**) combined profiles.

3.4. Micro-Hardness

The micro-hardness profiles across the weldments are presented in Figure 16a for CCGTAW and Figure 16b for PCGTAW. The HV values of the weld zone were higher than those of the base metal steel AISI 316 in both welded joints and are listed in Table 8. The hardness of WM lowered to 225 HV, which corresponded to CC. The decrease in hardness observed in the WM as heat input increased can be attributed to differences in the cooling rate as well as the phase fraction. Increasing the heat input resulted in a decrease in the cooling rate, which in turn encouraged the creation of γ-austenite [40]. This might have caused a decline in the hardness performance. The HV of the BM deteriorated in the HAZ of the weldments. This had the ability to impact the microstructure of the material, which could have resulted in variations in hardness. In addition, an elevated temperature can enhance the process of alloying and blending between the BM and the filler metal [41]. This can impact the dispersion of alloying elements and contribute to alterations in hardness. Elevated temperatures may also cause the weld and HAZ to have larger grain development, which could potentially lead to higher hardness [42]. Conversely, the magnitude of the distance between the roots might impact the dispersion of heat inside the area where the weld is formed [43]. An increased distance between the roots may lead to accelerated cooling, hence causing variations in hardness [12,26]. Figure 16c displays a comparison plot of CCGTAW and PCGTAW to verify the welding procedures and their impact on dissimilar weldments. The fluctuation in width, area, and HV may have been observed in both BMs, which could be related to the production of fine grain structures.

Table 8. Micro−hardness in various zones of CCGTAW and PCGTAW weldments.

Welding Technique	HAZ of SSDS 2507	Weld Zone	HAZ of AISI 316
CCGTAW	260	225	154
PCGTAW (4 Hz)	270	240	162

4. Conclusions

Experimental studies have been conducted on SSDS 2507 and AISI 316 weldments developed using CCGTAW and PCGTAW techniques with filler ER2205. From this study, the key findings are as follows:

- The fusion zone consisted of a high ferrite phase (δ) with a reformed austenite phase (γ) in the CCGTAW weldment, whereas balanced ferrite–austenite phases were observed in the PCGTAW weldment. Also, it was observed that the WM contained a higher amount of austenite compared to the HAZ and BM.
- The microstructures of both CCGTAW and PCGTAW weldments exhibited similar morphological characteristics, including GBA, inter-granular austenite, and Widmanstätten austenite, while the heat input had a major impact on the microstructure.
- A corrosion rate of 0.0487 mm/year was observed in the PCGTAW weldment, which was significantly better than that of the base metal (SSDS 2507 steel) and the CCGTAW weldment, which exhibited a corrosion rate of 1.3389 mm/year.
- In comparison to other pulse frequencies (2 Hz and 6 Hz) and the CCGTAW weldment, the tensile strength of PCGTAW at a 4 Hz pulse frequency produced higher weld strength (695 MPa).
- At 350 °C, the PCGTAW weld exhibited a strength of 475 MPa, which was greater than the strength of the CCGTAW weld, measured at 456 MPa.
- Higher hardness number was observed in the PCGTAW weldment (240 HV) due to the balanced ferrite–austenitic phase's structures in the weld zone compared to the CCGTAW weldment (225 HV).

Author Contributions: Conceptualization, M.V., B.Y., A.A. and M.O.D.; methodology, M.V. and M.I.; software, A.A., B.Y. and M.I.; validation, M.I., A.A., M.O.D., B.Y. and N.K.P.; formal analysis, M.V. and A.A.; investigation, M.V., B.Y. and A.A.; resources, S.V.K., N.K.P. and M.O.D.; data curation, M.I., A.A., B.Y., S.V.K. and M.O.D.; writing—original draft preparation, M.V., B.Y. and A.A.; writing—review and editing, N.K.P., M.I. and M.O.D.; visualization, B.Y., S.V.K., N.K.P. and M.I.; supervision, B.Y. and A.A.; project administration, M.I.; funding acquisition, M.O.D. All authors have read and agreed to the published version of the manuscript.

Funding: The APC was funded by the University of Johannesburg.

Data Availability Statement: All relevant data and results are presented within this manuscript.

Conflicts of Interest: The authors declare no conflicts of interest.

References

1. Soleimani, A.; Akbari, M.; Karimipour, A.; Meghdadi Isfahani, A.H.; Nosouhi, R. Investigation the Effect of Dissimilar Laser Welding Parameters on Temperature Field, Mechanical Properties and Fusion Zone Microstructure of Inconel 600 and Duplex 2205 Stainless Steel via Response Surface Methodology. *Heliyon* **2024**, *10*, e26010. [CrossRef] [PubMed]
2. Silva, C.M.; Leonard, K.J.; Garrison, L.M.; Bryan, C.D. Effects of Low-Temperature Neutron Irradiation on the Microstructure and Tensile Properties of Duplex 2304 Stainless Steel and Its Electron-Beam Welds. *Mater. Sci. Eng. A* **2021**, *823*, 141780. [CrossRef]
3. Xie, X.; Jiang, W.; Pei, X.; Niu, R.; Li, X.; Dong, Z.; Wan, Y.; Liu, B. Synthetical Effect of Material Inhomogeneity and Welding Defects on Fatigue Behavior of 2205 Duplex Stainless Steel Cruciform Welded Joints: Experiments and Life-Prediction Model. *Int. J. Fatigue* **2023**, *168*, 107472. [CrossRef]
4. Mohammed, G.; Ishak, M.; Aqida, S.; Abdulhadi, H. Effects of Heat Input on Microstructure, Corrosion and Mechanical Characteristics of Welded Austenitic and Duplex Stainless Steels: A Review. *Metals* **2017**, *7*, 39. [CrossRef]

5. Agarwal, A.; Mthembu, L. Numerical Modelling and Multi Objective Optimization Analysis of Heavy Vehicle Chassis. *Processes* **2021**, *9*, 2028. [CrossRef]
6. Gao, S.; Geng, S.; Jiang, P.; Mi, G.; Han, C.; Ren, L. Numerical Analysis of the Deformation Behavior of 2205 Duplex Stainless Steel TIG Weld Joint Based on the Microstructure and Micro-Mechanical Properties. *Mater. Sci. Eng. A* **2021**, *815*, 141303. [CrossRef]
7. Deng, B.; Jiang, Y.; Xu, J.; Sun, T.; Gao, J.; Zhang, L.; Zhang, W.; Li, J. Application of the Modified Electrochemical Potentiodynamic Reactivation Method to Detect Susceptibility to Intergranular Corrosion of a Newly Developed Lean Duplex Stainless Steel LDX2101. *Corros. Sci.* **2010**, *52*, 969–977. [CrossRef]
8. Zhang, L.; Jiang, Y.; Deng, B.; Zhang, W.; Xu, J.; Li, J. Effect of Aging on the Corrosion Resistance of 2101 Lean Duplex Stainless Steel. *Mater. Charact.* **2009**, *60*, 1522–1528. [CrossRef]
9. Han, Y.; Zhang, Y.; Jing, H.; Gao, Z.; Xu, L.; Zhang, Z.; Zhao, L. Microstructure and Corrosion Studies on Different Zones of Super Duplex Stainless Steel UNS S32750 Weldment. *Front. Mater.* **2020**, *7*, 100–110. [CrossRef]
10. Ouali, N.; Khenfer, K.; Belkessa, B.; Fajoui, J.; Cheniti, B.; Idir, B.; Branchu, S. Effect of Heat Input on Microstructure, Residual Stress, and Corrosion Resistance of UNS 32101 Lean Duplex Stainless Steel Weld Joints. *J. Mater. Eng. Perform.* **2019**, *28*, 4252–4264. [CrossRef]
11. Saravanan, S.; Sivagurumanikandan, N.; Raghukandan, K. Effect of Heat Input on Microstructure and Mechanical Properties of Nd: YAG Laser Welded Super Duplex Stainless Steel-Numerical and Experimental Approach. *Optik* **2019**, *185*, 447–455. [CrossRef]
12. Wang, Q.; Gu, G.; Jia, C.; Li, K.; Wu, C. Investigation of Microstructure Evolution, Mechanical and Corrosion Properties of SAF 2507 Super Duplex Stainless Steel Joints by Keyhole Plasma Arc Welding. *J. Mater. Res. Technol.* **2023**, *22*, 355–374. [CrossRef]
13. Giorjão, R.A.R.; Pereira, V.F.; Terada, M.; da Fonseca, E.B.; Marinho, R.R.; Garcia, D.M.; Tschiptschin, A.P. Microstructure and Mechanical Properties of Friction Stir Welded 8 Mm Pipe SAF 2507 Super Duplex Stainless Steel. *J. Mater. Res. Technol.* **2019**, *8*, 243–249. [CrossRef]
14. Devendranath Ramkumar, K.; Mishra, D.; Ganesh Raj, B.; Vignesh, M.K.; Thiruvengatam, G.; Sudharshan, S.P.; Arivazhagan, N.; Sivashanmugam, N.; Rabel, A.M. Effect of Optimal Weld Parameters in the Microstructure and Mechanical Properties of Autogeneous Gas Tungsten Arc Weldments of Super-Duplex Stainless Steel UNS S32750. *Mater. Des. 1980–2015* **2015**, *66*, 356–365. [CrossRef]
15. Tahchieva, A.B.; Llorca-Isern, N.; Cabrera, J.-M. Duplex and Superduplex Stainless Steels: Microstructure and Property Evolution by Surface Modification Processes. *Metals* **2019**, *9*, 347. [CrossRef]
16. Verma, J.; Taiwade, R.V. Effect of Welding Processes and Conditions on the Microstructure, Mechanical Properties and Corrosion Resistance of Duplex Stainless Steel Weldments—A Review. *J. Manuf. Process.* **2017**, *25*, 134–152. [CrossRef]
17. Yelamasetti, B.; Vardhan, T.V.; Ramana, G.V. Study of Metallurgical Changes and Mechanical Properties of Dissimilar Weldments Developed by Interpulse Current TIG Welding Technique. *Proc. Inst. Mech. Eng. Part C J. Mech. Eng. Sci.* **2021**, *235*, 2985–2997. [CrossRef]
18. Yelamasetti, B.; Kumar, D.; Saxena, K.K.; Rajyalakshmi, G. Experimental Investigation on Temperature Profiles and Residual Stresses in GTAW Dissimilar Weldments of AA5052 and AA7075. *Adv. Mater. Process. Technol.* **2022**, *8*, 352–365. [CrossRef]
19. Güzey, B.N.; İrsel, G. Investigation of Mechanical and Microstructural Properties in Joining Dissimilar P355GH and Stainless 316L Steels by TIG Welding Process. *Int. J. Press. Vessel. Pip.* **2023**, *205*, 104965. [CrossRef]
20. Atapek, Ş.H.; Tümer, M.; Çelikkol, E.; Kısasöz, A.; Kerimak, M.Z. Microstructural, Mechanical and Corrosion Behavior of UNS S31803/Hastelloy C-276 Dissimilar Metal Welds. *CIRP J. Manuf. Sci. Technol.* **2023**, *40*, 129–141. [CrossRef]
21. Jula, M.; Dehmolaei, R.; Alavi Zaree, S.R. The Comparative Evaluation of AISI 316/A387-Gr.91 Steels Dissimilar Weld Metal Produced by CCGTAW and PCGTAW Processes. *J. Manuf. Process.* **2018**, *36*, 272–280. [CrossRef]
22. Ramkumar, K.D.; Dagur, A.H.; Kartha, A.A.; Subodh, M.A.; Vishnu, C.; Arun, D.; Kumar, M.G.V.; Abraham, W.S.; Chatterjee, A.; Abraham, J.; et al. Microstructure, Mechanical Properties and Biocorrosion Behavior of Dissimilar Welds of AISI 904L and UNS S32750. *J. Manuf. Process.* **2017**, *30*, 27–40. [CrossRef]
23. Ramkumar, K.D.; Pranav, N.P.; Sai, B.; Arun, D.; Christin, S.V. Microstructure and Mechanical Integrity Relationship of PDC Weld Joints Involving Dissimilar Marine Grade Alloys. *J. Manuf. Process.* **2020**, *50*, 111–122. [CrossRef]
24. Song, I.; Jeong, G.-H.; Kim, S.-K.; Kim, Y.H.; Murphy, A.B.; Park, T.-K.; Kim, D.; Park, H.; Cho, D.-W. Effects of Autogenous Gas Tungsten Arc Welding (GTAW) on Corrosion Resistance of Stainless Steel 316L. *Processes* **2024**, *12*, 1757. [CrossRef]
25. Na, T.; Jeong, G.-H.; Kim, K.; Kim, Y.; Bae, J.; Kim, S.; Ahn, S.-H.; Bae, S.-H.; Kim, S.-K.; Cho, D.-W. Structural Analysis of Thermal Diffusion and Non-Uniform Temperature Distribution along the Sidewall Thickness of STS316L During Gas Tungsten Arc Butt Welding. *Processes* **2024**, *12*, 1038. [CrossRef]
26. Wang, S.; Mei, P.; Chang, L.; Wu, C.; Chen, S.; Chen, Q.; Li, G. Evaluation of the Corrosion Resistance of 904L Composite Plate in a High-Temperature and High-Pressure Gas Field Environment. *Processes* **2024**, *12*, 2372. [CrossRef]
27. Ahmed, M.; Javidani, M.; Maltais, A.; Chen, X.-G. Comparison of Mechanical, Fatigue, and Corrosion Properties of Fusion-Welded High-Strength AA6011 Alloy Using Three Filler Wires. *Processes* **2024**, *12*, 1172. [CrossRef]

28. Ramkumar, K.D.; Goutham, P.S.; Radhakrishna, V.S.; Tiwari, A.; Anirudh, S. Studies on the Structure–Property Relationships and Corrosion Behaviour of the Activated Flux TIG Welding of UNS S32750. *J. Manuf. Process.* **2016**, *23*, 231–241. [CrossRef]
29. Alwin, B.; Lakshminarayanan, A.K.; Vasudevan, M.; Vasantharaja, P. Assessment of Stress Corrosion Cracking Resistance of Activated Tungsten Inert Gas-Welded Duplex Stainless Steel Joints. *J. Mater. Eng. Perform.* **2017**, *26*, 5825–5836. [CrossRef]
30. Karhu, M.; Kujanpää, V. Gas Tungsten Arc Process Optimization and Assessment for Robotized Position Welding of Austenitic Stainless Steel Edge Joints. *CIRP J. Manuf. Sci. Technol.* **2022**, *36*, 12–22. [CrossRef]
31. Yelamasetti, B.; Karuna, B.N.R.; Vishnu Vardhan, T.; Dasore, A.; Saxena, K.K.; Faroque, F.A.; Revathi, V.; Abduvalieva, D. Mechanical and Micro-Structural Studies of Pulsed and Constant Current TIG Weldments of Super Duplex Stainless Steels and Austenitic Stainless Steels. *High Temp. Mater. Process.* **2024**, *43*, 177–187. [CrossRef]
32. Pai, A.; Sogalad, I.; Kumar, P.; Basavarajappa, S.; Suresha, S.J. Impact Properties of Modified 9Cr 1Mo Steel Welds: Comparison between Cold Wire and Hot Wire Gas Tungsten Arc Welding Processes. *Int. J. Press. Vessel. Pip.* **2022**, *198*, 104672. [CrossRef]
33. Han, J.; Wang, Y.; Lan, L.; Shao, C.; Lu, F. Precipitate Evolution and Its Effect on Corrosion Properties of Different Weld Joints for Al-Mg-Er Alloy. *Mater. Lett.* **2023**, *351*, 135089. [CrossRef]
34. Yelamasetti, B.; Ramana, G.V.; Sanke, N.; Gupta, N. Numerical and Experimental Residual Stress Analysis of Dissimilar Metals of Inconel 718 and AISI 316 Developed in GTAW Process. *Int. J. Interact. Des. Manuf. IJIDeM* **2024**, *18*, 2093–2105. [CrossRef]
35. Agarwal, A.; Mthembu, L. Comparative Analysis of Boron-Al Metal Matix Composite and Aluminum Alloy in Enhancing Dynamic Performance of Vertical-Axis Wind Turbine. *Processes* **2024**, *12*, 2288. [CrossRef]
36. Sonar, T.; Balasubramanian, V.; Venkateswaran, T.; Xavier, V.; Muthumanickam, A.; Manjunath, A.; Ivanov, M.; Suleymanova, I. Effect of Post Weld Heat Treatment on Weld Metal Microstructure and Hardness of HFCA-TIG Welded ASTM-B670 High Temperature Alloy Joints. *J. Alloys Metall. Syst.* **2023**, *3*, 100025. [CrossRef]
37. Li, Z.; Samuel, A.M.; Samuel, F.H.; Ravindran, C.; Valtierra, S. Effect of Alloying Elements on the Segregation and Dissolution of $CuAl_2$ Phase in Al-Si-Cu 319 Alloys. *J. Mater. Sci.* **2003**, *38*, 1203–1218. [CrossRef]
38. Kumar, S.; Kumar, Y.; Vimal, K.E.K. Microstructural and Corrosion Behavior of Thin Sheet of Stainless Steel-Grade Super Duplex 2507 by Gas Tungsten Arc Welding. *SAE Int. J. Mater. Manuf.* **2024**, *17*, 135–144. [CrossRef]
39. Grewal, R.; Aranas, C.; Chadha, K.; Shahriari, D.; Jahazi, M.; Jonas, J.J. Formation of Widmanstätten Ferrite at Very High Temperatures in the Austenite Phase Field. *Acta Mater.* **2016**, *109*, 23–31. [CrossRef]
40. Han, L.; Han, T.; Chen, G.; Wang, B.; Sun, J.; Wang, Y. Influence of Heat Input on Microstructure, Hardness and Pitting Corrosion of Weld Metal in Duplex Stainless Steel Welded by Keyhole-TIG. *Mater. Charact.* **2021**, *175*, 111052. [CrossRef]
41. Chandrasekar, V.; Ramkumar, K.D. Effect of Nb-Free Consumables on the Microstructure and Structural Integrity of Pressure Vessel Grades of Dissimilar Austenitic Stainless Steel Welded Joints. *J. Mater. Res. Technol.* **2022**, *18*, 3443–3456. [CrossRef]
42. Ma, Y.; Su, L.; Shen, C.; Fletcher, L.; Li, H.; Sun, L.; Zheng, L.; Zhang, C. Improving the Weld Heat-Affected-Zone (HAZ) Toughness of High-Strength Thick-Walled Line Pipes. *Metals* **2023**, *13*, 2018. [CrossRef]
43. Bunaziv, I.; Langelandsvik, G.; Ren, X.; Westermann, I.; Rørvik, G.; Dørum, C.; Danielsen, M.H.; Eriksson, M. Effect of Preheating and Preplaced Filler Wire on Microstructure and Toughness in Laser-Arc Hybrid Welding of Thick Steel. *J. Manuf. Process.* **2022**, *82*, 829–847. [CrossRef]

Disclaimer/Publisher's Note: The statements, opinions and data contained in all publications are solely those of the individual author(s) and contributor(s) and not of MDPI and/or the editor(s). MDPI and/or the editor(s) disclaim responsibility for any injury to people or property resulting from any ideas, methods, instructions or products referred to in the content.